Acta Materialia, AM 16430

In situ neutron diffraction investigation of texture-dependent Shape Memory Effect in a near equiatomic NiTi alloy

Zifan Wang[a], Jingwei Chen[a], Cyril Besnard[a], Lenka Kuncicka[b], Radim Kocich[b], Alexander M. Korsunsky[a,*]

[a] *MBLEM, Department of Engineering Science, University of Oxford, Oxford OX1 3PJ, U.K.*
[b] *Faculty of Materials Science and Technology, VŠB-Technical University of Ostrava, Ostrava 8, Czech Republic*

*Corresponding author. E-mail address: alexander.korsunsky@eng.ox.ac.uk

DOI: https://doi.org/10.1016/j.actamat.2020.10.049

Received 6 July 2020, Revised 8 October 2020, Accepted 21 October 2020, Available online 27 October 2020.

Abstract

To explore the possibility of customising the functional behaviour of NiTi shape memory alloy via controlling texture, binary $Ni_{55}Ti_{45}$ (wt.%) alloys were manufactured in *as cast* and *hot swaged* conditions, presenting contrasting initial texture and macroscopic performance. *In situ* time-of-flight neutron diffraction technique was employed to study the texture effect on the microstructural evolution during Shape Memory Effect (SME), and a range of properties were evaluated. It was found that (i) hot swaging process leads to change in grain morphology and increase in microstrain; (ii) thermal expansion coefficients of martensite and austenite variants were weakly affected by the texture and phase transformation constraint; (iii) significant texture effect on the elastic properties at both macro- and micro-scale was quantified by Elasto-Plastic Self-Consistent (EPSC) modelling approach, while the anisotropic elastic moduli lie within the range for single crystal state and twinned structure; (iv) texture evolution during SME is weakly related to the initial microstructure; (v) grains reoriented so that the <010> axis became aligned parallel to the loading direction, and retained this orientation upon unloading, revealing the underlying correlation between texture evolution and detwinning. Based on the experimental results, a multi-variant model was proposed to quantify the lattice strain evolution during SME. Validity of the conceptually simple and parametrically parsimonious model was confirmed by validation against experimental data.

Keywords:

Bespoke NiTi Shape Memory Alloys, Texture, Shape memory effect, EPSC, *In situ* neutron diffraction

1.Introduction and objectives

Probably the most important category of shape memory materials that exhibit useful functional behaviour under specific stimuli, Shape Memory Alloys (SMAs) have been widely utilized in

applications of medical actuators, aerospace, micromechanical systems, and the elastocaloric cooling devices that recently come into fashion [1]. Among the three extensively developed and used alloy systems, namely NiTi-based, Cu-based and Fe-based, the binary NiTi always remain the first choice in engineering applications due to its excellent thermomechanical performance and biocompatibility.

Two widely utilised functional types of behaviour of NiTi are Superelasticity (SE) and Shape Memory Effect (SME). The latter lies in the focus of interest for the present study. To induce SME, deformation begins at a critical temperature below M_f. When stress is applied, the martensite (M) phase deforms pseudo-plastically through self-accommodated twinning to detwinning process, showing pronounced macroscopic strain up to ~8%. After stress is withdrawn, detwinned martensite retains its shape until being heated above critical temperature A_s, at which the reverse phase transformation to austenite (A) initiates. The full strain recovery is reached above A_f temperature.

Over the years, numerous investigations attempted to identify and clarify the underlying crystallographic mechanisms that affect SME in NiTi alloys. The contribution of elastic strain was studied for different forms of NiTi, including single crystal and twinned structure, through ultrasonic measurements [2], first-principles calculations [3], and other computational modelling approaches [4,5]. The investigation of pseudo-plastic strain, namely the stress-induced detwinning, elucidated the mechanism from various aspects of energetics [6,7], microstructural characterisation [8,9,10,11], thermodynamics [12,13] and texture evolution [4,14].

These studies lay a solid foundation to the understanding of mechanisms of SME. However, recent research demonstrated that the actual SME performance of NiTi alloy is greatly influenced by thermomechanical processing methods that produce NiTi products of different shapes, dimensions and microstructure in terms of phase composition [12], internal strain field [15], crystallite morphology [16] and texture [17,18].

The aforementioned studies and others not reported here appear to have failed to address systematically the texture effect on SME from the microscopic point of view. The subject was

somewhat superficially investigated in a limited number of studies, most of which were based on *ex situ* rather than *in situ* analyses, so that the details of the microstructural evolution during SME remain to be explored.

In situ time-of-flight (TOF) neutron diffraction (ND) may be the most advantageous technique in probing the mesoscale volume-averaged deformation response of microstructure, since neutron beams penetrate several millimetres deep into the material, thus providing highly reliable statistical data from bulk polycrystalline samples [11,14,19]. Most importantly, the technique allows the extraction of refined crystallographic information from diffraction spectra, including reflection-dependent lattice *d*-spacings, grain orientation, and phase volume fraction evolution that is essential to evaluate the morphological and mechanical texture effect on the microstructural evolution during SME [20,21]. Furthermore, accurate quantification of macroscopic deformation response of NiTi alloy requires attendant and supportive models that consider various properties such as microstrain, orientation- and phase-dependent thermal expansion coefficients, elastic moduli, texture, and so on. However, the experimental data related to these factors is scarce.

Having identified the significance of this topic and the boundary of existing knowledge, the objective of this work is to study the texture-dependent SME in NiTi alloy using *in situ* TOF neutron diffraction analysis. NiTi samples of contrasting initial texture were manufactured via two conditions, namely as cast (AC) and hot swaging (HS). Experimental efforts were aimed at evaluating grain morphology, microstrain, thermal expansion coefficients, lattice strain evolution, elastic properties, and texture evolution. Based on the experimental observations, the texture effect on lattice strain evolution was quantified via EPSC and a novel multi-variant model. Being the likely first attempt of this kind so far, the potential outcome of the present study aims to give guidance in customising the functional behaviour in NiTi alloy by means of controlling different textures.

Note that in this study, the term “variant” is equivalent to *hkl* grain groups or *hkl* reflections, which correspond to the diffraction peaks in the ND spectrum [4,11,15,16,19].

2.Experimental and analytical procedures

2.1 Material processing methodology

For raw material, nickel cubes of 4N purity and commercially pure (>99.3%) Grade 2 titanium were used. A polycrystalline $Ni_{55}Ti_{45}$ wt.% ϕ 20mm rod was cast into an iso-statically pressed graphite crucible via vacuum induction melting (VIM) at 150 Mbar under Argon atmosphere of 6N purity.

The as cast rod was split into two pieces, one of which was subjected to hot rotary swaging at 950°C (see Ref. [22,23] for details on manufacturing). Rotary swaging is a versatile industrially applicable technology that reduces diameter of the processed axisymmetric workpiece by incrementally imposing intensive shear strain via a set of four rotating dies, as shown in Fig. 1. The three swaging passes were performed and monitored by the KOMAFU S600 system developed by us [24,25]. With the diameter reduced to ϕ12mm, the as cast (AC) and hot swaged (HS) rods present contrasting texture (Fig. 12 & 13).

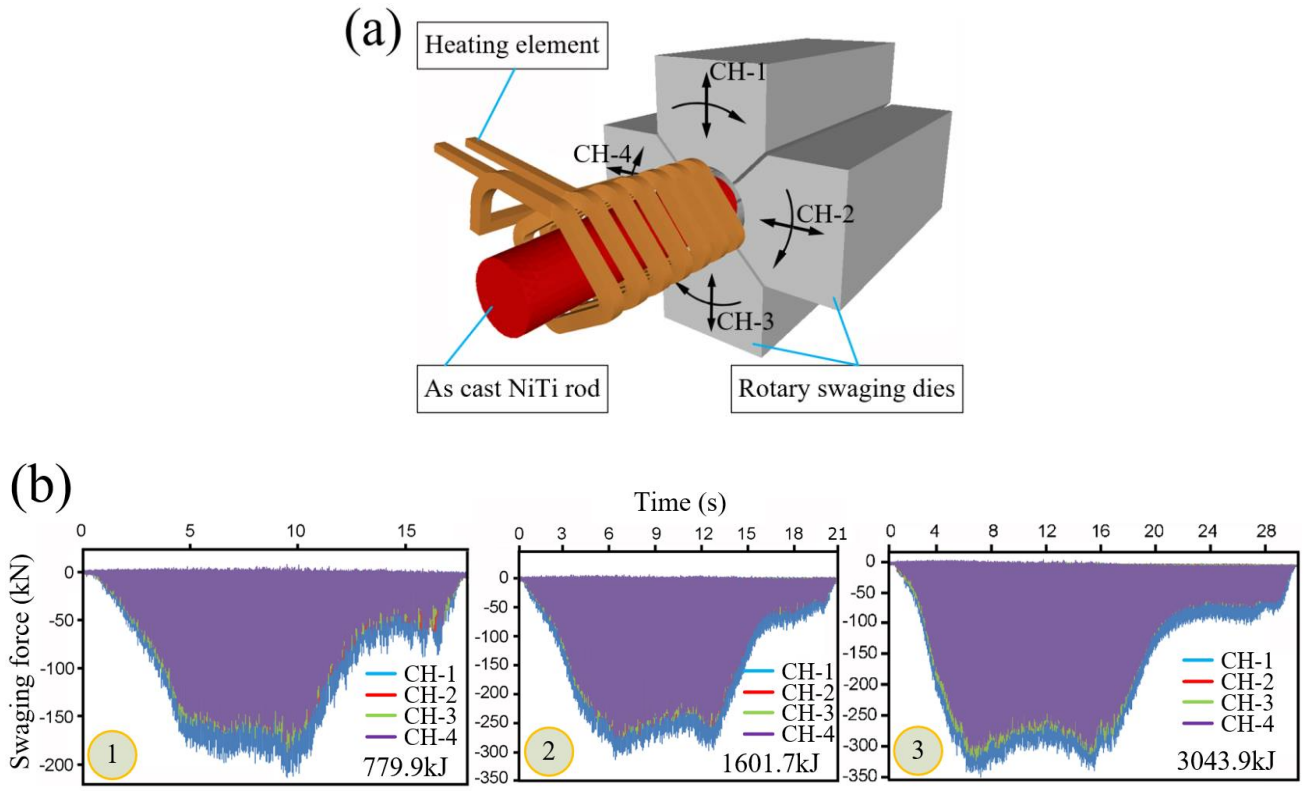

Fig. 1. Three-step hot rotary swaging using four pressing dies (a). The corresponding deformation work of each step was recorded in unit of kJ (b).

2.2 DSC analysis

To determine the deformation and recovery temperature of SME, stress-free transformation temperatures were measured by a TA DSC Q2000 differential scanning calorimetry (DSC) instrument in the wide temperature range between -90°C and 200°C to cover the complete transformation process. During the test, the samples were first cooled down to -90°C and stabilized for 2 min, then cycled two loops to ensure consistent experimental result. The ramp rates for heating / cooling were both 5°C/min. Result is shown in Fig. 2.

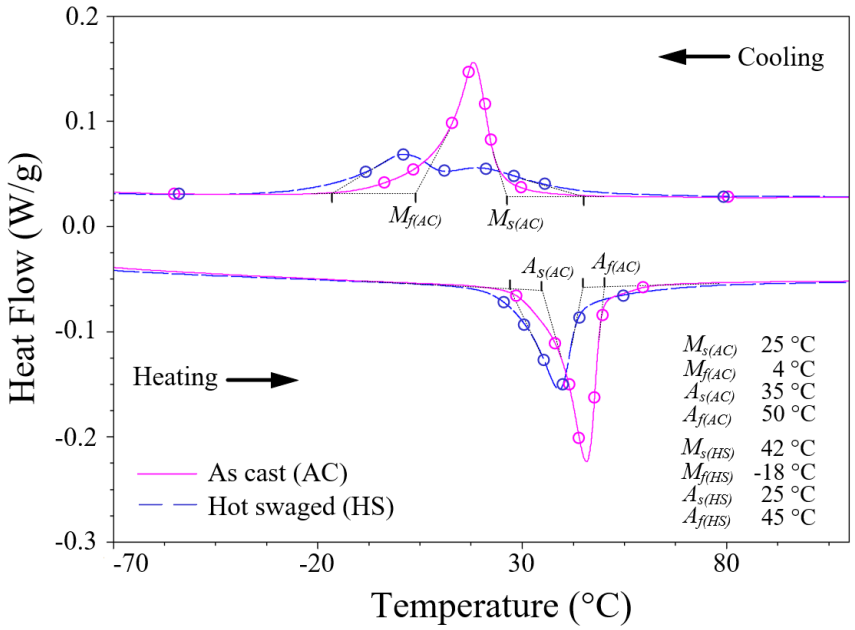

Fig. 2. The measured values of critical phase transformation temperatures, definitions refer to the introduction [12]. Circles denote the temperatures at which stress-free ND measurements were performed.

2.3 EBSD Characterization

To assess the change in grain morphology after thermomechanical processing, electron backscatter diffraction (EBSD) observations were carried out in a Tescan LYRA3 system integrated with a SYMMETRY EBSD detector from Oxford Instruments. Samples were polished down to a final step of 0.25μm colloidal silica and heated to induce the cubic austenite phase. Kikuchi pattern indexing was performed at an accelerating voltage of 20kV, a working distance of 9mm, a step size of 0.12μm, and an acquisition speed of 7Hz.

2.4 Neutron diffraction experiments

In situ time-of-flight (TOF) neutron diffraction experiments were conducted using the pulsed spallation source at ISIS, Rutherford Appleton Laboratory managed by Science & Technology Facilities Council (STFC) in the UK. ENGIN-X beamline is a 50m flight path instrument equipped with a 50kN hydraulic loading rig custom-built by Instron. The cryobox, capable of cooling and heating in a range of -200 to 100°C, was attached to the rig. During operation, the box chamber was pumped vacuum ($<10^{-4}$ Pa) to ensure homogenous temperature distribution on the specimen. An extensometer was clamped in the middle for macroscopic strain measurement.

The loading frame was horizontally arranged in such a way that the loading direction is 45° relative to the incident beam, with two opposing $\mp$90°detector banks whose span angular ranges $\mp$7° in both horizontal and vertical directions. The beam spot size defined by radial collimators was 4×4mm throughout the experiment. Setup illustration is shown in Fig. 3. Additional details in [26,27].

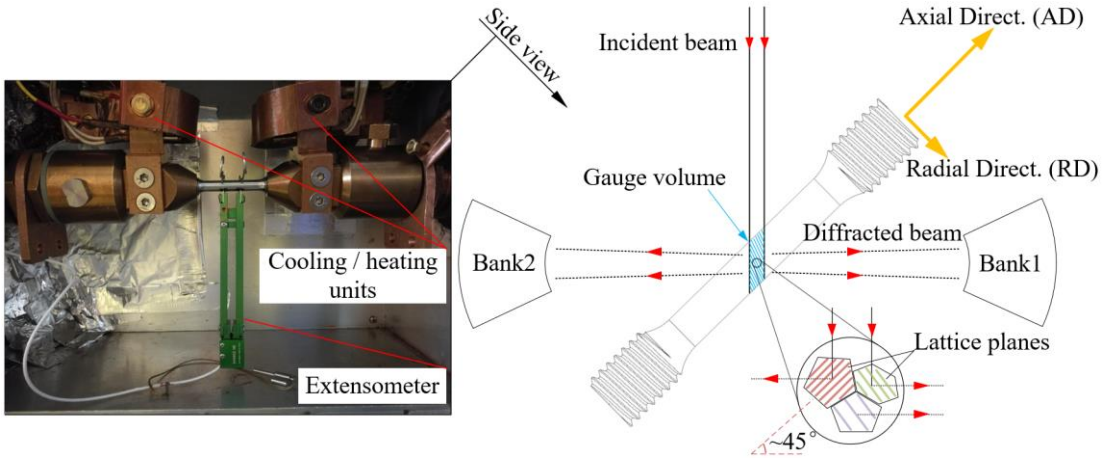

Fig. 3. Side view photograph (left). The sketch of setup from top view (right). Note that specimen coordinate is defined by the orthogonal AD and RD axes.

Prior to the ND experiment, the rods were machined into cylindrical dog-bone specimens with a gauge diameter of 6mm. The scheme of stress-free thermal cyclic test is shown in Fig. 2. To ensure virgin state, a new sample of each type was used for SME. Samples were maintained at -35°C during the uniaxial tensile loading / unloading with a strain rate of $1\times10^{-4}s^{-1}$. Upon unloading to zero stress,

the sample was gradually heated to 85°C to induce shape recovery. At each measurement point, the sample was held at a constant strain for ~43 minutes to collect spectra of adequate statistical quality. The scheme of ND during the SME process is shown in Fig. 4.

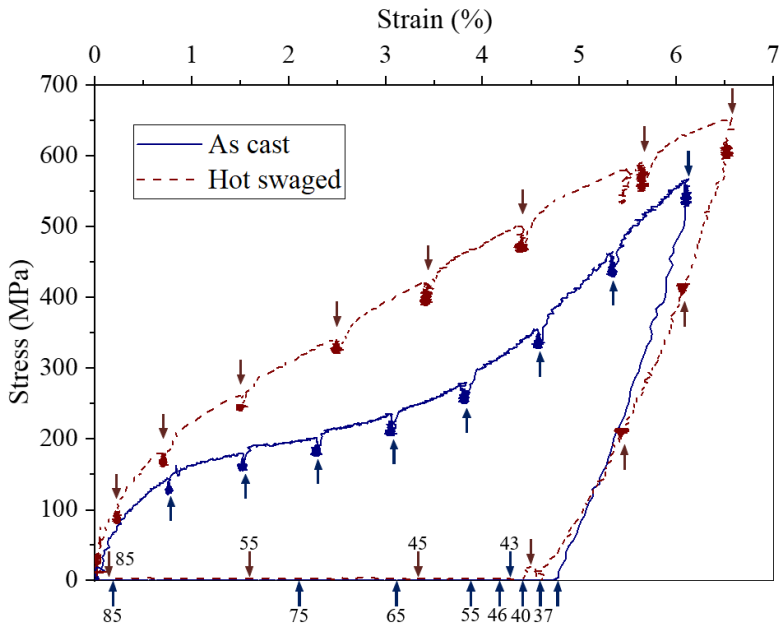

Fig. 4. Macroscopic SME response of both samples. Arrows denote the strain levels at which the samples were held for ND data acquisition. Digits in small font indicate corresponding temperatures during strain recovery upon heating, otherwise at -35°C. Stress relaxations of approximately 10MPa are considered negligible.

2.5 Neutron diffraction spectra analysis

In the first instance, data were analysed using Rietveld refinement technique [28] implemented in the General Structures and Analysis System (GSAS) code [29]. Based on a least-squares scheme that minimizes the differences between the theoretical and experimental spectra, the method allows the refinement of phase fractions, lattice parameters, lattice strains, texture, etc., that are averaged in the gauge volume. As a metric of goodness of fit, the typical χ^2 value in this study is ~0.9, which is considered decent. The initial crystal structure for calculation of theoretical spectrum is referred to [30]. As shown in Fig. 14, one of the two conventions describing NiTi monoclinic structure is adopted in the analysis of spectra data, such that c-axis as the diad axis and γ as the non-orthogonal angle, consistent with [4,30,31]. An example of refined spectrum is shown in Fig. 5.

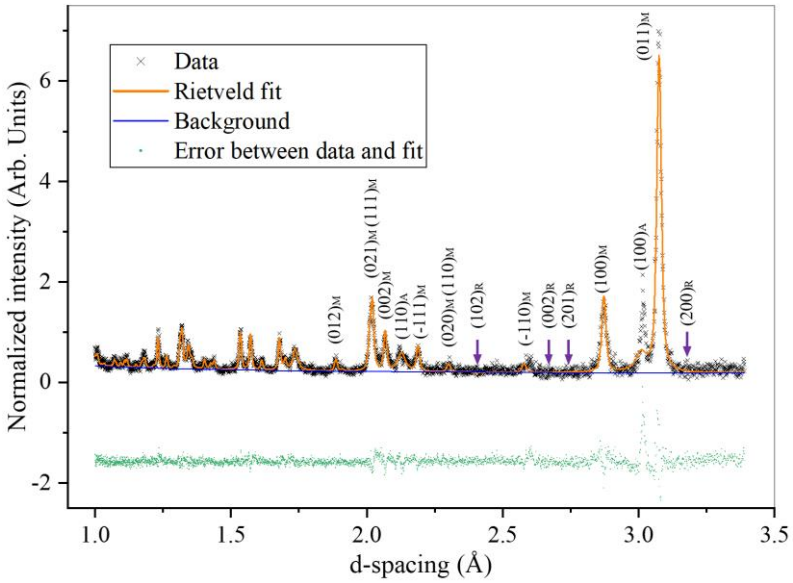

Fig. 5. Refined and indexed spectrum at 10°C during thermally induced phase transformation from austenite (A) to martensite (M) of hot swaged NiTi (AD). Peak positions for low index *hkl* variants are marked for A, M and R-phase.

In the second instance, Pseudo-Voigt single peak fitting method imbedded in ENGIN-X analysis routine [32] was used to compute lattice strains of individual *hkl* variants parallel to the axial loading direction (AD) and radial direction (RD), as illustrated in Fig. 3.

Furthermore, the texture evolution was captured using analysis procedures outlined in [33]. Raw pole figures were constructed from the refined 6th order spherical harmonics in GSAS, assuming cylindrical symmetry of texture produced by the symmetric rotary swaging process. The orientation distribution functions (ODFs) were then reconstructed using MTEX software [34]. Hence the plotted inverse pole figures (IPFs) enable tracking the texture in the axial (AD) and radial (RD) direction of the cylindrical gauge volume [4].

3.Experimental results and discussion

3.1 Microstructural evolution

3.1.1 Grain morphology

EBSD analysis is shown in Fig. 6. The compressive and shearing force of hot swaging induces the heterogeneity in grain morphology in such a way that grains at the outer radius of cross section

were heavily deformed with their dimension along RD reduced, while the grain at the inner region retain the equi-axed shape analogous to the as cast rod. From a macroscopic point of view, the ovality of grain shape increases after hot swaging, which coincides well with observation from the EPSC modelling approach in section 3.3.3.

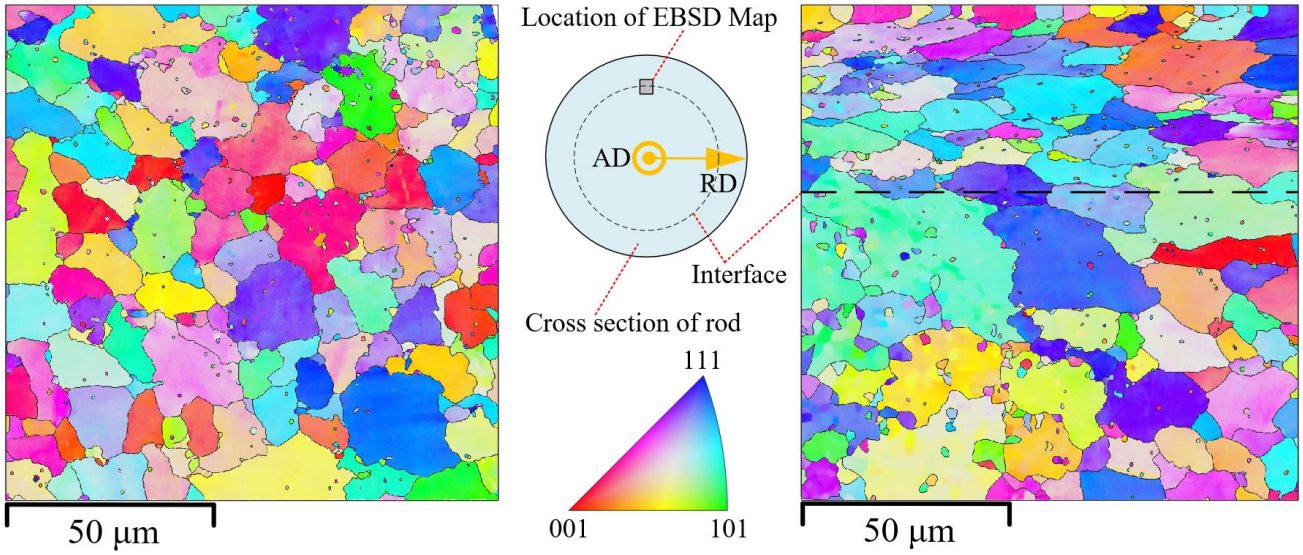

Fig. 6. Colour-coded inverse pole figure maps on cross-section of as cast (left) and hot swaged (right) NiTi rods. The triangular colour key indicates grain orientations parallel to the axial direction (AD). Location of the two EBSD maps was carefully selected so as to exhibit the interface that reveals the grain morphology heterogeneity in the HS rod.

3.1.2 Microstrain

The peak profile of austenite phase of AC and HS NiTi are shown in Fig. 7a.

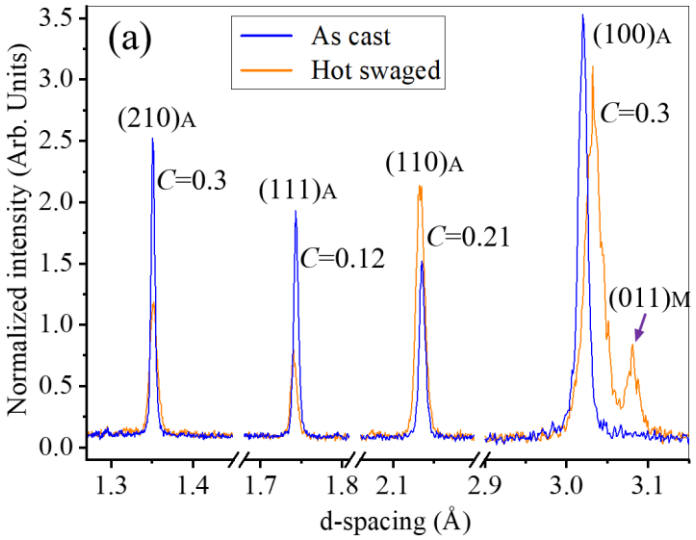

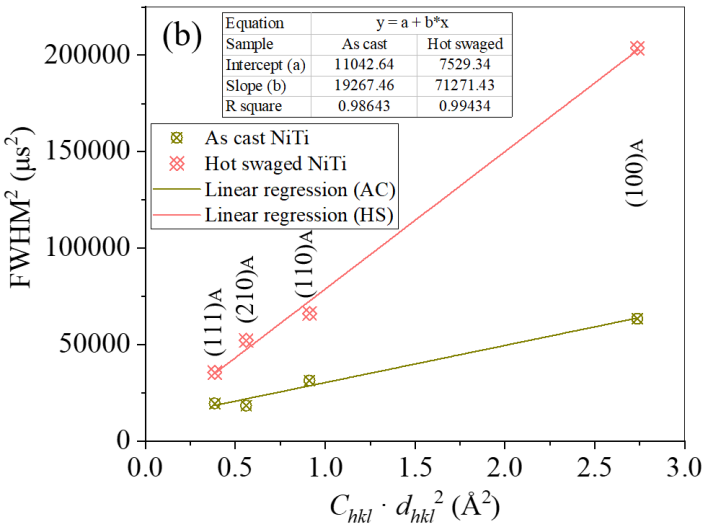

Fig. 7. (a) The comparison of peak profile of cubic austenite phase at 80°C. (b) A modified W-H plot, the slope of the linear fittings contain information of the microstrain in AC and HS NiTi. The uncertainties of $FWHM^2$ are comparable to the size of plotted symbols.

To evaluate the change in microstrain caused by hot swaging, the full width at half maximum (FWHM) of the observed diffraction peaks can be deconvoluted into multiple contributions from instrument response (Δd_{ins}), grain size (Δd_{size}) and microstrain (Δd_{ε}) through Fourier transformation [35]. Consider the strain expression as $\varepsilon=\Delta d_{\varepsilon}/d_{hkl}$, which directly reveals the non-uniform lattice deformation from $d_{hkl}+\delta d$ to $d_{hkl}-\delta d$ for a specific *hkl* variant. Note that the microstrain induced by lattice defects is assumed to be homogeneously distributed among variants. The effect of elastic anisotropy in B2 cubic austenite phase in NiTi alloy can be eliminated via introducing the contrast factors *C* [36], so that we obtain:

$$FWHM^2 = \Delta d_{ins}^2 + \Delta d_{size}^2 + \Delta d_{\varepsilon}^2 = \Delta d_{ins}^2 + \Delta d_{size}^2 + \varepsilon^2 d_{hkl}^2 C, \quad (1)$$

where d_{hkl} is the d-spacing of an *hkl* plane (peak profile centre). The calculated *C* values for each *hkl* are marked in Fig. 7a, details refer to [36]. Eq. (1) is a typical $y=a+bx$ equation, *a* being the intercept and *b* the slope. This modified Williamson-Hall approach provides information on the microstrain (ε^2) from the slope of the plot, as shown in Fig. 7b. The fitting parameters are listed in the inset. It can be qualitatively concluded that the hot swaging process brings about a significant increase in non-uniform lattice deformation (microstrain), which is mostly associated with lattice defects.

3.2 Thermal expansion of martensite & austenite

To study the texture effect on thermal expansion, the hydraulic loading rig was set to stress control at 0 MPa during thermal cycling, therefore the samples can move freely in the loading direction, allowing the measurement of both macroscopic and microscopic phase transformation strain. The extensometer data shows that the variation of macroscopic shape-change strain is less than 0.1% after formation of nascent phase during cooling / heating. This suggests the accommodative nature of the twinned M phase, wherein the elastic, thermal and allotropic mismatch is minimised [37].

Mesoscopic thermal expansion of variants can be obtained from lattice strains, which are quantified via the shifts in positions of individual *hkl* reflections:

$$\varepsilon_{hkl} = \frac{d^{hkl} - d_0^{hkl}}{d_0^{hkl}}, \tag{2}$$

where d_0^{hkl} and d^{hkl} denote the *d*-spacing of specific *hkl* at initial state and after thermomechanical deformation, respectively. Using Eq. (2), the lattice strains of M and A are determined, as plotted in Fig. 8. The relative rather than absolute strains are considered in the analyses.

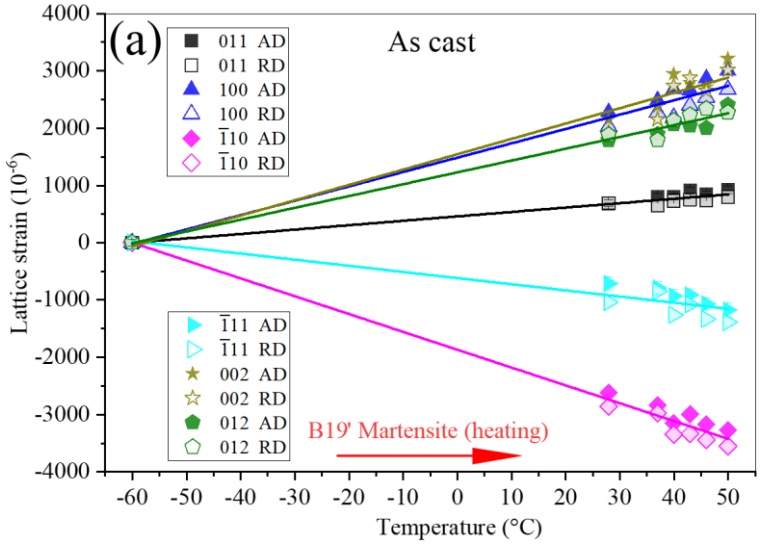

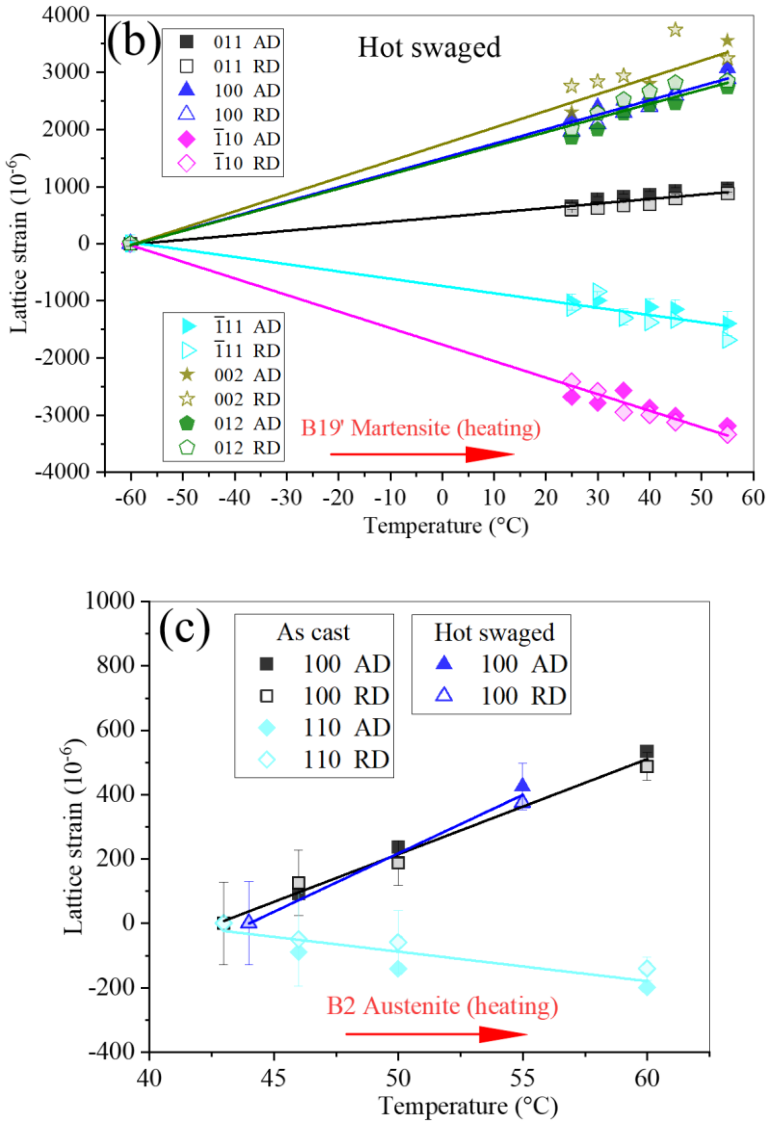

Fig. 8. Lattice strain as a function of temperature upon heating. As cast (a) and hot swaged (b) NiTi martensite phase. NiTi austenite phase (c). Linear regression is performed for each variant. Uncertainties are displayed either as error bars or comparable to the size of plotted symbols.

It is noteworthy that the thermal expansion in both M and A phases retain a good linearity throughout the heating process, including the phase transformation process (10-60°C, according to DSC). Whilst the variation in coefficient of thermal expansion in *hkl* variants is attributed to anisotropy arising from crystal symmetry, the linearity suggests the accommodative nature of M phase and its capability to selectively transform to A, thereby minimising the intergranular stress between M and A grains.

The coefficient of thermal expansion of *hkl* variants can be obtained from linear fit in Fig. 8, and

listed in Table 1. It is also worth mentioning that unlike the significant effect of texture on elastic properties which is discussed in the next section, the coefficients of thermal expansion are relatively independent of texture, since their values are similar between AC, HS and hot-drawn [37] NiTi. Components of thermal expansion tensor can be further determined using the values in Table 1, details refer to [37].

The measured thermal expansion coefficients of variants are used to compensate thermal expansion effect in the calculation of lattice strain during shape recovery in section 3.4.

Table 1
Coefficient of thermal expansion of NiTi martensite and austenite variants.

Unit:10^{-6}/°C	011_M	100_M	-110_M	-111_M	002_M	012_M	100_A	110_A
As cast	7.7	25.1	-30.2	-10.7	26.8	20.6	29.6	-9.2
Hot swaged	7.9	25.3	-29.0	-12.7	29.3	23.7	32.3	

3.3 *In situ* neutron diffraction of SME

The overview of SME ND spectra is shown in Fig. 9, the evolution of which exhibits the difference in microstructural behaviour between AC and HS NiTi. Detailed analyses are in the sections below.

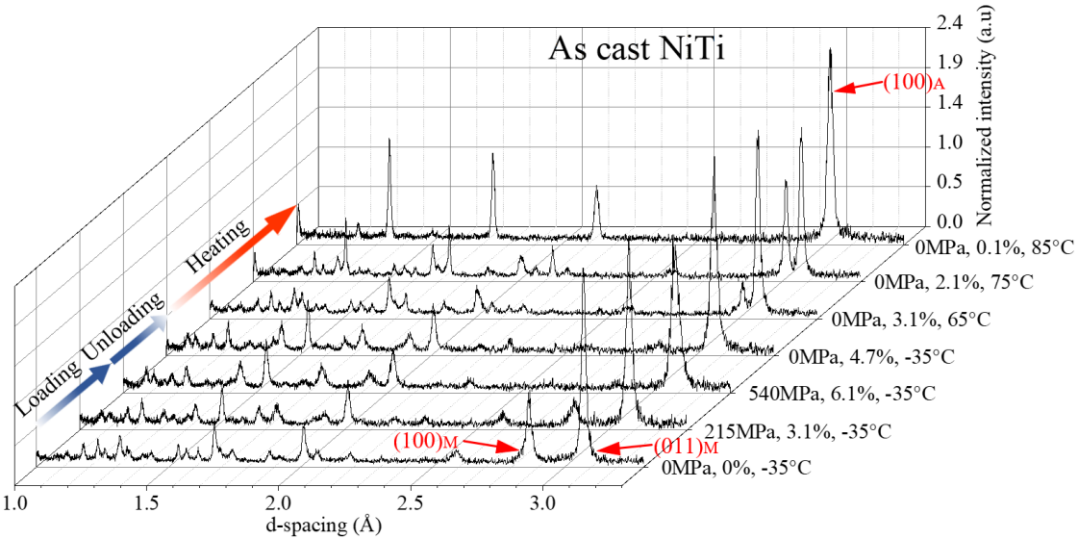

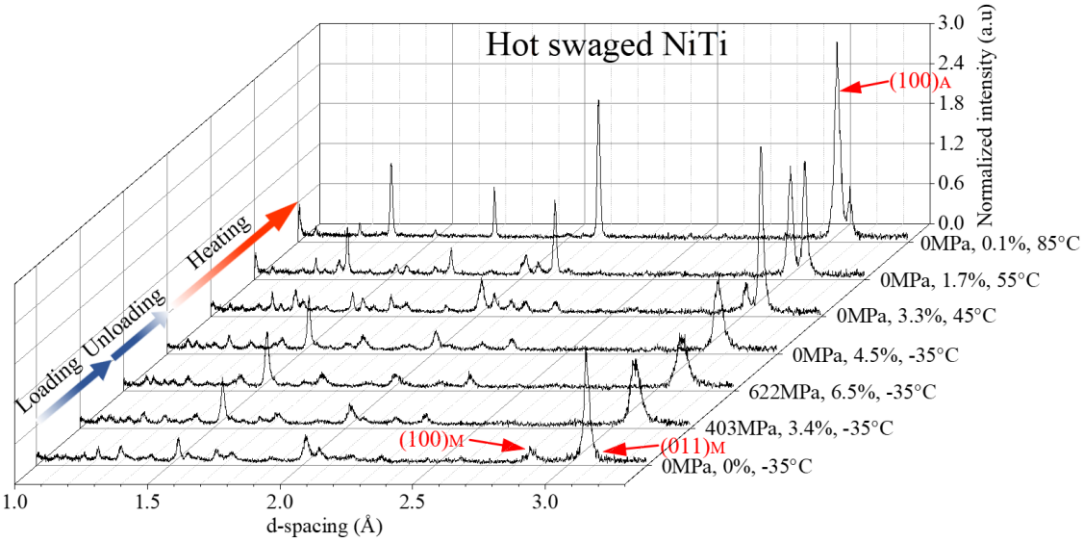

Fig. 9. The overview of spectra of AC and HS NiTi during SME, corresponding stress, strain and temperature of each spectrum are recorded on the right. Detailed peak index refers to Fig. 5 and Fig. 7a.

3.3.1 Lattice strain evolution

The shifts in positions of individual peaks can be converted into lattice strains of *hkl* variants using Eq. (2), the evolution of which is shown in Fig. 10. The lattice strain shown here are from variants whose *hkl* plane normal are parallel to the AD and RD (Fig. 3). It should be noted that these variants are freely distributed around the normal of scattering *hkl* planes since this does not interfere with the Bragg's condition. This means that the strains perceived from individual peaks are peculiar average from a subset of all grains in the gauge volume.

During the SME tensile loading, the integrated intensity of some reflections gradually decrease to zero, for example, (100), (-110) and (121) in AD of both samples. Since the integrated intensity of an individual peak is proportional to the number of grains involved in the diffraction, the disappearance of the peak is caused by the rotation of these grains and hence the interference of Bragg condition. This phenomenon can also be intuitively viewed from the peak profiles in Fig. 9. The general observation here is that the grain reorientation tend to favour those variants with either relatively low or high stiffness compared with the average level, for instance, AC (-110) and (012) in AD, (110), AC (020) and (-120) in RD, HS (121) and (002) in AD, thus interacting with the matrix and rotating.

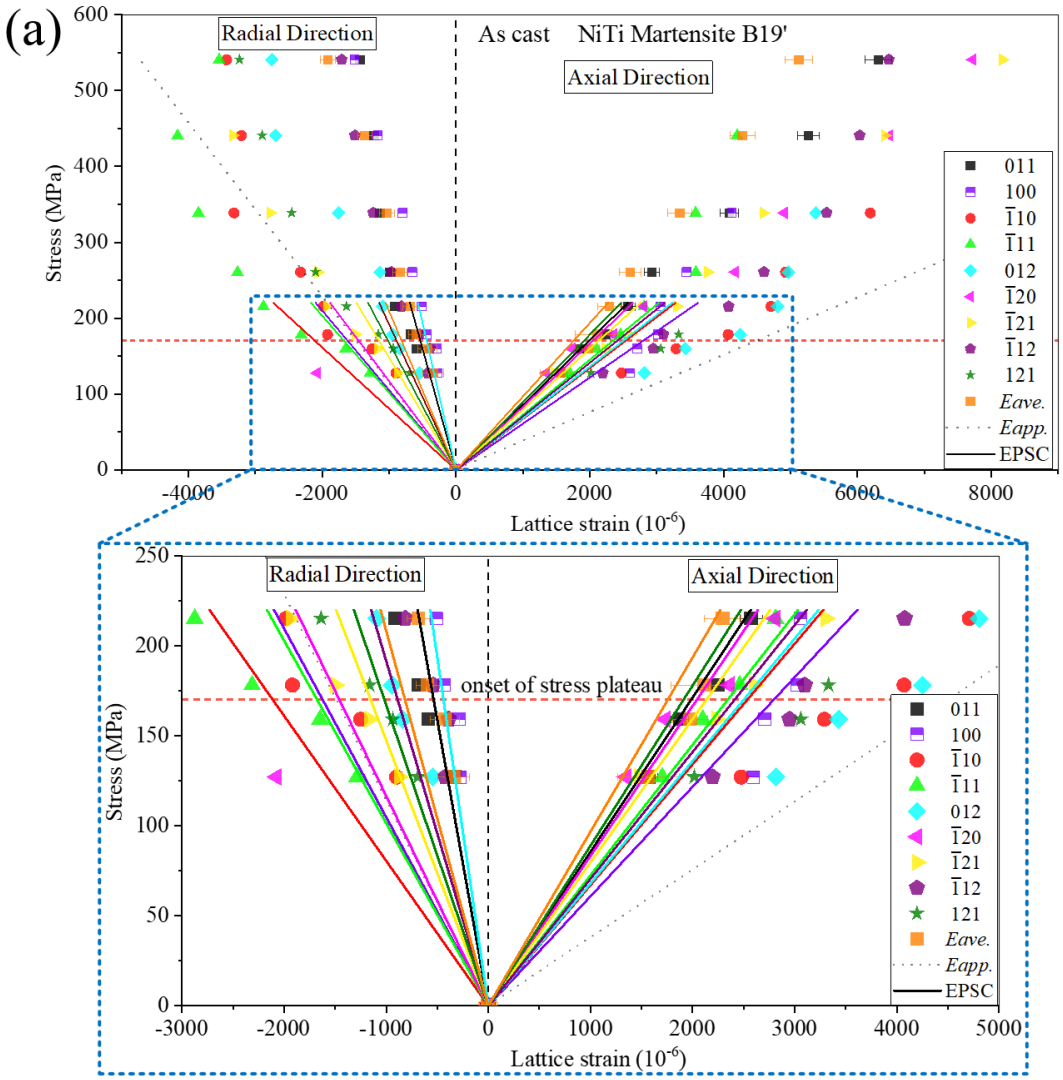
(a)
Radial Direction
As cast NiTi Martensite B19'
Axial Direction
Stress (MPa)
Lattice strain (10^{-6})
011
100
$\bar{1}10$
$\bar{1}11$
012
$\bar{1}20$
$\bar{1}21$
$\bar{1}12$
121
Eave.
Eapp.
EPSC
onset of stress plateau

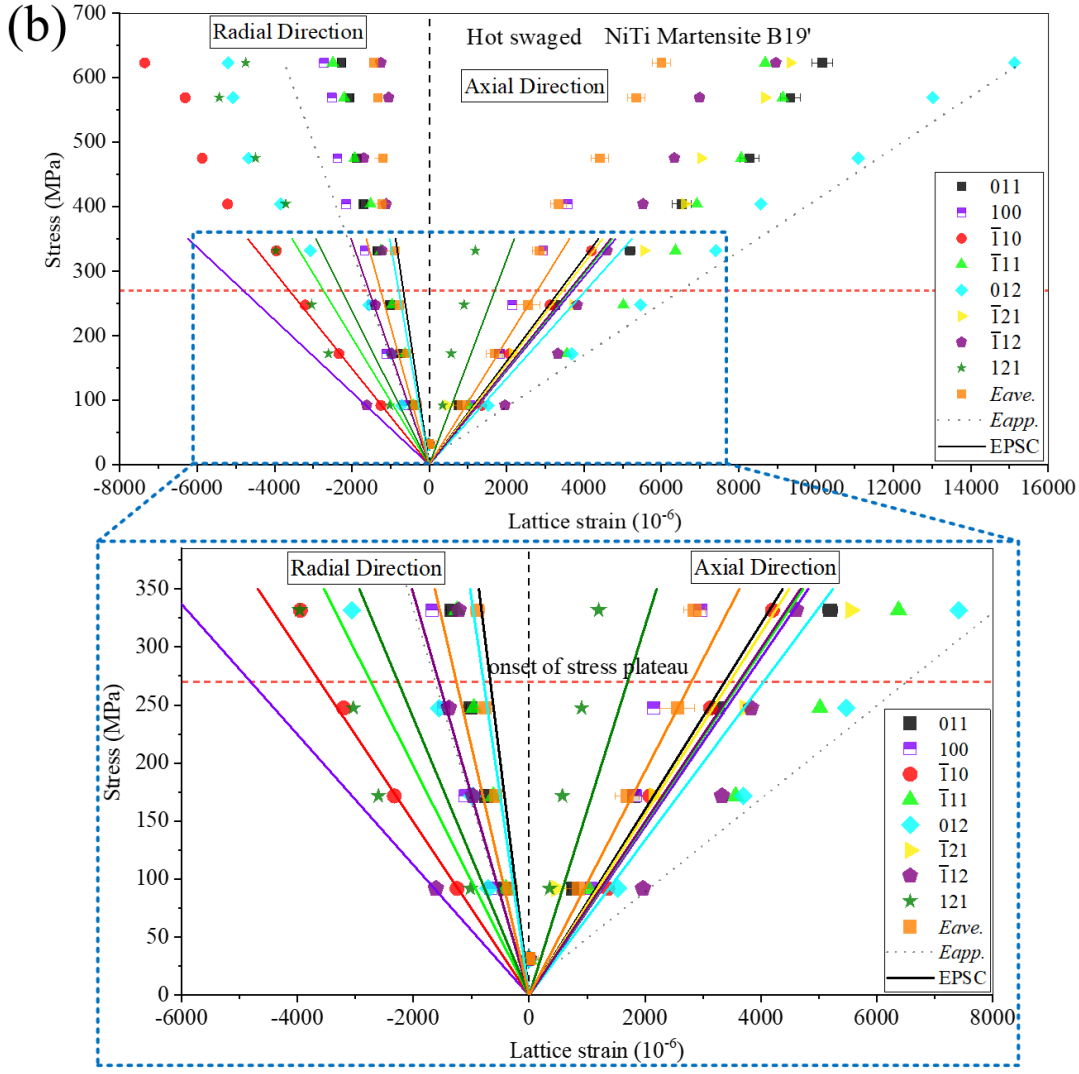

Fig. 10. The lattice strain evolution of AC (a) and HS (b) martensitic NiTi during loading. Typical uncertainties are displayed for (011), those of other variants are of similar magnitude. EPSC simulation of elastic response of each variant is drawn in solid lines using the same colour.

3.3.2 Elastic properties

Apparent elastic moduli ($E_{app.}$) were determined from the gradient of initial slopes of the tensile stress-strain curves. Rietveld refinement method can be used to evaluate a volume averaged elastic modulus ($E_{ave.}$) in polycrystalline materials [4]. The elastic strain associated with a lattice plane, ε_{hkl}, can be described incorporating isotropic and anisotropic contributions with two fitting parameters, α and β:

$$\varepsilon_{hkl} = \varepsilon_{isotropic} - \varepsilon_{anisotropic} = \frac{\alpha}{C} - \frac{\beta \cdot \cos\phi}{C}, \quad (3)$$

where C is a diffractometer constant. α fits peaks in spectrum by varying the lattice parameters (a,

b and c) such that $\Delta a/a = \Delta b/b = \Delta c/c$, thus capturing the isotropic strain. β accounts for the anisotropy component. For a given *hkl*, ϕ is the angle between the plane normal and [100] for martensitic NiTi. Following the refinement using Eq. (3), $E_{ave.}$ can be obtained by setting β to zero.

Theoretical elastic moduli of variants can be calculated for two extreme states of the martensite phase, namely the single crystal and twinned structure. Single crystal without internal twinning is known to possess the highest stiffness while the presence of twinned structure would significantly reduce the value [5]. Therefore, the twinned structure may represent the martensite at its lowest stiffness. For martensite NiTi, the elastic modulus E_{hkl} in the direction perpendicular to a *hkl* plane can be calculated using equation [38]:

$$E_{hkl} = (l_1^4 S_{11} + 2l_1^2 l_2^2 S_{12} + 2l_1^2 l_3^2 S_{13} + 2l_1^3 l_3 S_{15} + l_2^4 S_{22} + 2l_2^2 l_3^2 S_{23} + 2l_1 l_2^2 l_3 S_{25} + l_3^4 S_{33} + 2l_1 l_3^3 S_{35} + l_2^2 l_3^2 S_{44} + 2l_1 l_2^2 l_3 S_{46} + l_1^2 l_3^2 S_{55} + l_1^2 l_2^2 S_{66})^{-1}, \quad (4)$$

where S_{ij} are the 13 independent compliance constants obtained through DFT simulation, given in [5] for both single crystal and twinned structure.

Determined by least square linear fit of data points, values of $E_{app.}$, $E_{ave.}$, E_{hkl} are listed in Table 2. The experimental results from a hot drawn NiTi rod are also included for comparison.

Table 2

Values of E_{hkl}, E_{app} and $E_{ave.}$ from both experiment and EPSC, together with Hill-average elastic moduli from DFT simulation are listed. Poisson ratios (v) are calculated by dividing E_{hkl} in RD into that in AD. Expt. stands for experiment.

hkl	As cast NiTi				Hot swaged NiTi				Hot drawn NiTi [4]	Single crystal	Twinned structure
	E_{hkl}		v		E_{hkl}		v		E_{hkl}	E_{hkl}	E_{hkl}
	Expt.	EPSC	Expt.	EPSC	Expt.	EPSC	Expt.	EPSC			
011	85.4	85.6	0.31	0.21	63.7	80	0.23	0.08	117.1	183.9	60.5
100	69.2	64.4	0.18	1.2	100.5	72.7	0.59	1.34	132.2	152.6	26
-110	52.5	69.2	0.39	0.85	78.9	74.4	0.87	0.9	78.2	169	23.4
-111	92.2	74.2	0.95	0.89	58.2	74.7	0.23	0.76	104.7	76.2	11.2
012	52.3	72.6	0.27	0.08	41.3	67.1	0.36	0.07	145.4	159.7	40.3
-120	68.8	80.2	0.78	0.69					101.4	150.8	35.4
-121	69	78.7	0.44	0.47	67.5	78.1			93.3	98	21.1

-112	72.9	73.5	0.23	0.4	74.8	76.6	0.27	0.41	165.1	79.4	20.2
121	62.8	88.2	0.41	0.34	366	105.4	3.45	1.41	104.6	120.1	31.7
$E_{app.}$	37.8				55				50		
$E_{ave.}$	99.7	96.84	0.31	0.44	107.4	98.6	0.32	0.51	134		
E_{DFT}										180($v =$ 0.31)[29]	71($v =$ 0.35)[5]

$E_{ave.}$ of HS NiTi is higher than that of AC NiTi, while the hot drawn (HD) NiTi is the highest. These experimental results of $E_{ave.}$ agree well with DFT simulation, all within the range of 71-180 GPa. This indicates that the AC NiTi contains the original amount of twinned structures while those in HS and HD samples were detwinned due to the compressive forming process. The averaged Poisson ratios from experiment and DFT are similar (~0.31-0.35) regardless of the microstructure.

The values of E_{app} (37.77-55 GPa) are consistent with those reported in previous studies (40-70 GPa) and has been mistakenly considered to be the actual martensite modulus of NiTi in many literatures. The fact is that the real elastic modulus $E_{ave.}$ is more than two times the value of $E_{app.}$. This confusing dilemma of elastic modulus implies that considerable amount of martensite twins are inelastically detwinned before the onset of stress-plateau [39,40].

The experimental results of E_{hkl} lie within the range of single crystal and twinned structure. However, few exceptions exist such as the E_{-111} of AC NiTi and E_{121} of HS NiTi, which suggests that the intergranular constraint arising in polycrystalline materials exerts non-negligible influence on the anisotropic elasticity. The abnormal value of Poisson ratio (>0.5) is another evidence of the effect. Therefore, EPSC simulation that takes into account the influence of microstructure, was carried out to quantify the elastic response of variant.

3.3.3 EPSC quantification of elastic properties

The Elasto-Plastic Self-Consistent (EPSC) approach was employed to simulate the effect of texture and grain morphology on anisotropic elastic response of variants. Based on Eshelby theory, the model treats each variant as an ellipsoidal inclusion embedded in a homogeneous medium. Numerical

implementation is described in [41].

Grain population files (Fig. 11) were generated consistent with the texture observed from ND. The simulation parameters, namely ellipsoid ratios and elastic constants were tuned to fit the experimental result of AC NiTi. Then the grain population file was substituted by that of HS NiTi to verify the texture effect. Parameters are listed in Table 3.

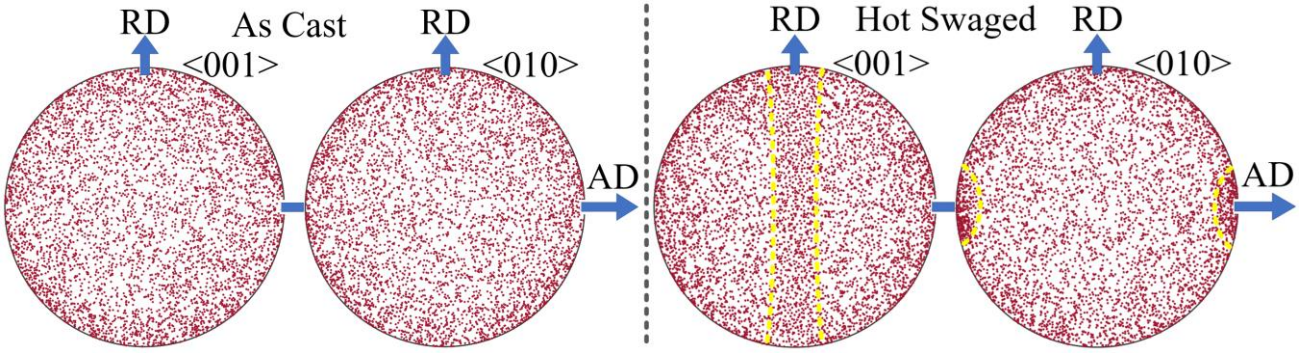

Fig. 11. Orientation of 6000 grains among 12000 that used in EPSC simulation. Yellow dashed line highlights the enhanced fibre texture in grain population file.

Table 3
EPSC simulation parameters.

	Ellipsoid Ratios			C_{11}	C_{12}	C_{13}	C_{14}	C_{22}	C_{23}	C_{25}	C_{32}	C_{35}	C_{44}	C_{46}	C_{55}	C_{66}
	x	y	z													
AC	0.4	1.2	2	35	102	120	1	135	120	27	80	7	67	5	13	52
HS	0.4	1.2	20													

Most variants exhibit crooked stress-strain response above the onset of stress plateau, as indicated by dashed line in Fig. 10. This non-linear behaviour in the stress-strain curve is mainly attributed to plastic deformation of variants from twinned to detwinned structure [4], hence simulation results is plotted in the elastic regime. Numerical comparison between experiment and EPSC result refers to Table 2.

This EPSC simulation demonstrates the texture-dependent elastic properties of variants. Furthermore, the effect of grain morphology was confirmed by the ellipsoid ratios in Table 3, in that the higher ovality of HS NiTi agrees well with the EBSD observation in Fig. 6.

3.3.4 Texture evolution

Fig. 12&13 are IPFs of AC and HS NiTi, respectively. The first IPF is plotted in full spherical space to illustrate the symmetry arising from the monoclinic crystal structure, indicating that only half circle is necessary to present a full map of texture. For the sake of clarity in comparison of textures in different directions and samples, all figures adopt the equal range of scale bar from 0-5, in units of m.r.d. (multiples of random distribution).

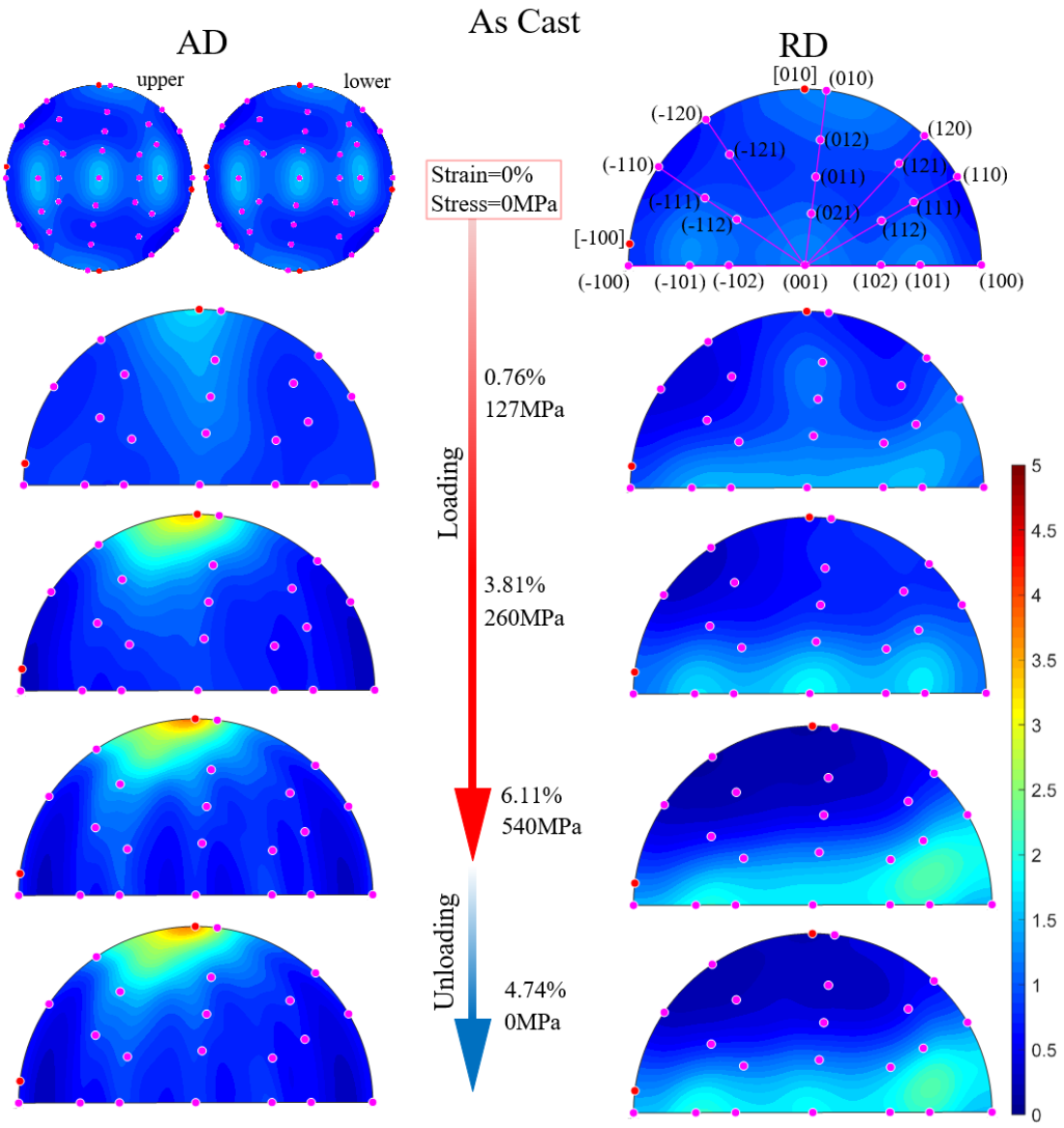

Fig. 12. Inverse pole figures (IPFs) of AC NiTi. The corresponding stress and strain levels are indicated in the middle. The *hkl* variant of low index are marked with pink dots. Four directions, namely <100> and <010> are drawn in red dots for reference.

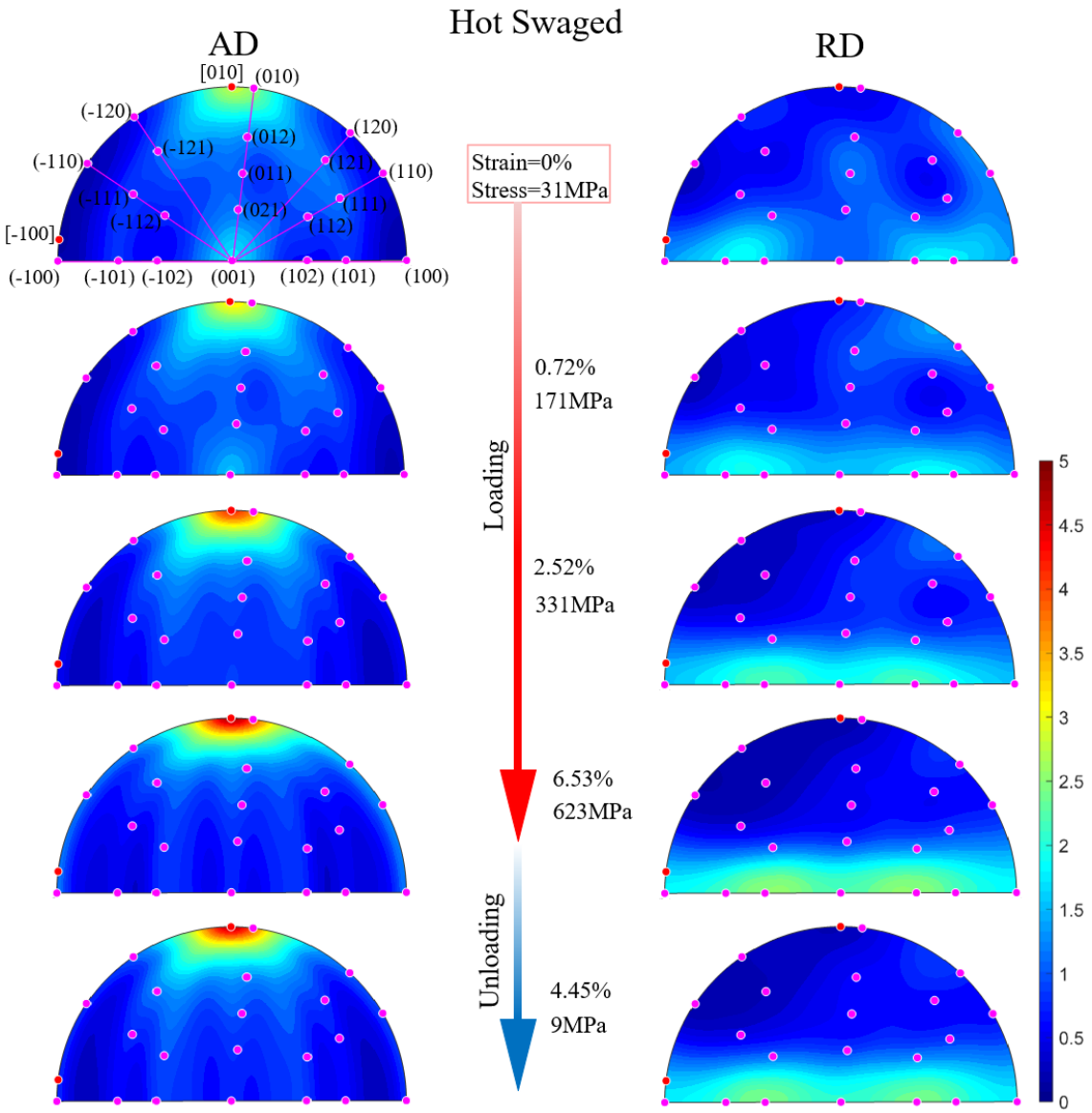

Fig. 13. IPFs of HS NiTi.

The initial texture of AC NiTi is weak, consistent with the low value of texture index of 1.32 (AD) and 1.13 (RD) obtained by Rietveld method. At virgin state, the texture distributions in two directions are similar that the density of (-101), (101), (001) and (010) are slightly higher. In comparison, HS NiTi exhibits distinct initial texture that the density of (010) in AD and (-101,101) in RD are around 2.8 m.r.d and 1.9 m.r.d., respectively.

With the gradual increase of applied stress, the majority of variants in AC NiTi are rearranged in such a way that the [010] direction (i.e. b-axis) being parallel to the axial loading direction and (-101), (001) and (101) being perpendicular. However, the texture rearrangement of both banks tends to

saturate at the stress level of 260MPa and above, corresponding to the end of stress-plateau in the macroscopic curve. The maximum density near [010] direction in AD merely increases from 3.7 to 3.9 m.r.d. upon the stress increment from 260 to 540 MPa. This means that major part of texture evolution takes place within the region of stress plateau. It may be inferred from the phenomenon that the texture evolution is closely correlated to detwinning process, since the grains reorient in such a way to accommodate the detwinning strain of (010) compound twins and (100) compound twins in the loading direction, as illustrated in Fig. 14. This inference and the observation of macroscopic SME curves suggests that the prevalent detwinning modes are related to both the <011> Type II twin and (010) & (100) compound twin [42], and the rearrangement of compound twins and others (e.g. <2-10> twin) after the plateau may be trivial in contribution to deformation [43]. Upon unloading from maximal stress to zero, the evolved texture does not show an obvious evidence of recovery, implying that the grain reorientation is inelastic.

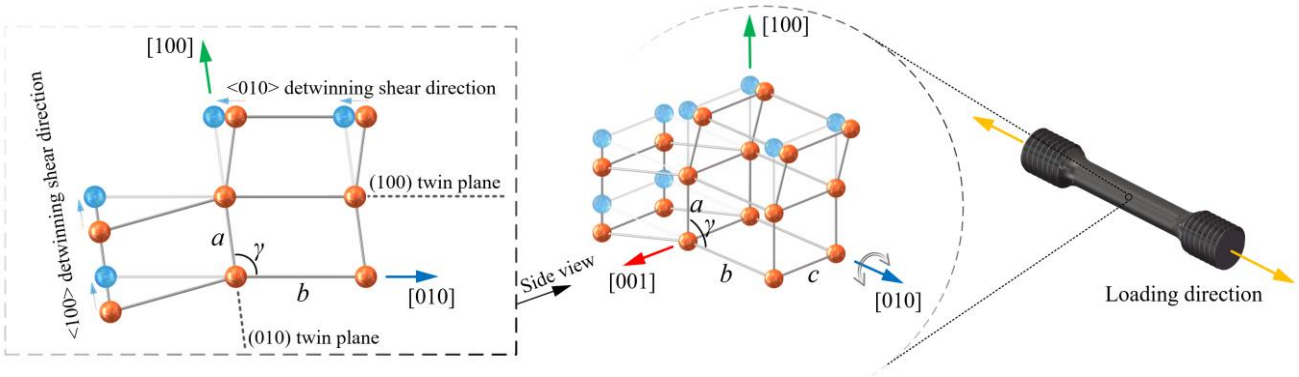

Fig. 14. Schematic illustration of detwinning of the (010) & (100) compound twin structures of martensite B19' NiTi. The texture information from IPFs indicate that grains reorient with the [010] direction parallel to the loading direction and distribute homogeneously around the [010] pole, thus accommodating the detwinning shear strain along the loading direction.

The texture evolution of HS NiTi is very similar to that of AC NiTi, except that the density reaches ~4.9 m.r.d. at maximal stress. Nevertheless, the higher density is attributed to the advantage of initial texture in HS sample rather than better adaptability of grains, since the variation in [010] density in AC NiTi (~2.9 m.r.d.) is higher than HS NiTi (~2.1 m.r.d.). Surprisingly, the texture evolution of AC

and HS samples are not only similar but also has a good agreement with those reported in other studies [4,44] using NiTi samples of different composition and processing methods. Hence it may be qualitatively assumed that the texture evolution in NiTi during SME is largely independent of initial microstructure. Besides, it should be noted that texture evolution takes place in AC and HS sample at low stress (~100 MPa), consistent with TEM studies [39,43] that the pseudo-plastic deformation starts in the "elastic regime" of deformation, which strongly supports the discussion in section 3.3.1 and 3.3.2.

3.4 Quantification of lattice strain evolution

The lattice strain evolution in NiTi can be captured by a "bi-crystal model", the concept of which was proposed in [16]. As illustrated in Fig. 15(a), the model is based on the assumption of anisotropic hybrid deformation in variants whose elongation are equally constrained by the boundary along the loading axis. Suppose two variants A and B having the same length (Step 1). Although both variants are martensite phase, they exhibit different modes of elastic and plastic deformation due to the anisotropy when external stress is applied (Step 2). In this case, the deformation of variant A may contain more inelastic component (i.e. pseudo-plastic detwinning and plastic slip) than B. Therefore, after unloading the difference in inelastic deformation results in the residual lattice strain distribution in the two grains (compression in A and tension in B), and hence the residual stress (σ_r) (Step 3). Upon heating, the detwinned martensite transforms to austenite such that the pseudo-plastic deformation (green colour) is recovered, causing the redistribution of lattice strain and residual stress (σ_r') due to the change of inelastic deformation in A and B (Step 4).

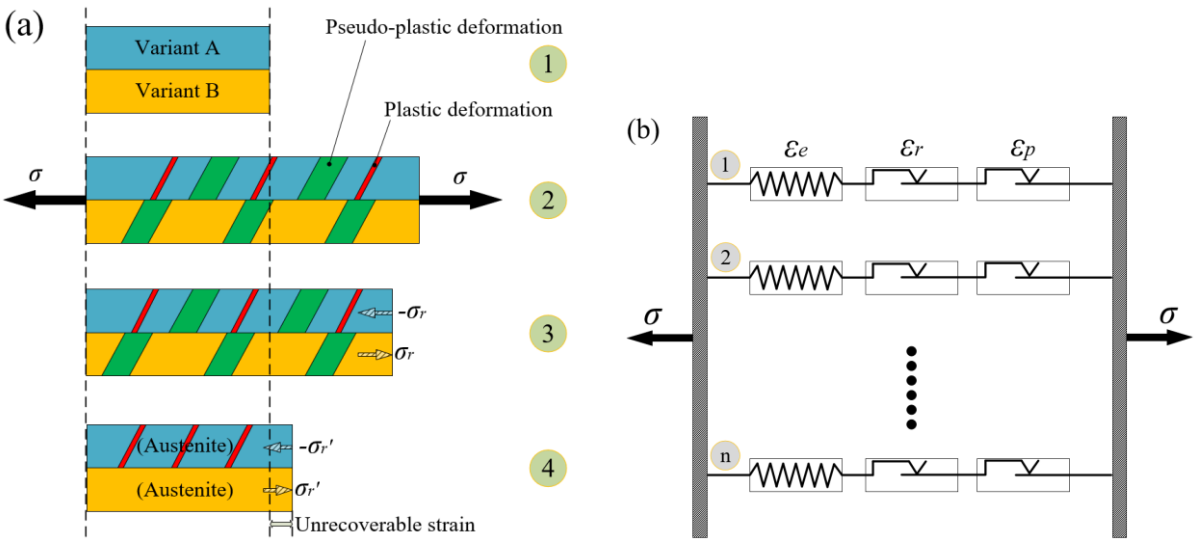

Fig. 15. The conceptual sketch of four deformation steps during SME of the bi-crystal model (a). Its generalized version proposed in this study (b).

The bi-crystal model can be further generalized to an assemblage of *N* elasto-plastic *hkl* variants connected in parallel, as shown in Fig. 13(b). The deformation of each variant is comprised of three strain modes, namely lattice strain (i.e. elastic strain) (ε_e), plastic strain (ε_p) and pseudo-plastic strain (i.e. recoverable strain) (ε_r). Assuming that the total strain (ε_t) of variants are equally constrained by the boundary on both sides, in that $\varepsilon_t = \varepsilon_e + \varepsilon_p + \varepsilon_r$. ε_t is the only independent variable, while ε_e is the dependent variable that this model aims to quantify.

The elastic strain of a variant can be given as: $\varepsilon_e = \sigma / E_{hkl}$, where σ and E_{hkl} are the applied stress and elastic property of the variant in loading direction, respectively. The value of σ corresponds to a given ε_t from the macroscopic stress-strain curve (Fig. 4), whilst the value of E_{hkl} is known from the texture-dependent EPSC results in section 3.3.2. Detwinning and phase transformation strain are considered to be the underlying mechanisms of shape recovery [45], whilst the latter can be neglected in this case because the phase transformation strain from twinned martensite to austenite is typically less than ~0.1%, which has been confirmed by stress-free thermal cycling in section 3.2. Therefore, the pseudo-plastic strain ε_r is equivalent to the martensite detwinning strain that can be

further split into two components:

$$\varepsilon_r = \varepsilon_{Type\ II} + \varepsilon_{Compound}, \tag{5}$$

where $\varepsilon_{Type\ II}$ denotes the detwinning strain of <011> Type II twins and $\varepsilon_{Compound}$ is that of compound twins. Given that the twining shear strain for (010) & (100) twin systems are equivalent [43], only the (010) compound twin is considered in the model. Details of these dominant twinning modes have been elucidated in [39,42,43,45,46].

In the process of detwinning, one variant of the CVP (Correspondence Variant Pair, denoting a martensite plate contains two twin-related martensite single-crystal variants) grows in the expense of the other, finally resulting in a single crystal of martensite. $\varepsilon_{Type\ II}$ can be calculated by:

$$\varepsilon_{Type\ II} = \sum_{n=1}^{24} \xi^n (\lambda^n - \lambda_0^n) R \mathbf{P}_{dt}^n R^T, \tag{6}$$

where λ^n is volume fraction of one variant (that of the other is $1-\lambda^n$) after detwinning. λ_0^n is the initial value [47]. Hence the term $\lambda^n - \lambda_0^n$ denotes the amount of transition between the two variants. ξ^n is the volume fraction of nth CVP in the matrix. R^T is the transpose of R, the strain transformation tensor that transforms the detwinning strain tensor $\mathbf{P}_{dt}^n$ from the original coordinate system to the direction of *hkl* normal:

$$R = \begin{bmatrix} \cos\alpha\cos\beta & \cos\alpha\sin\beta & \sin\alpha \\ -\sin\alpha\cos\beta & -\sin\alpha\sin\beta & \cos\alpha \\ \sin\beta & -\cos\beta & 0 \end{bmatrix}, \tag{7}$$

where $\alpha = \tan^{-1}(h/k)$, $\beta = \tan^{-1}\left((1.01l + 0.12h)/\sqrt{h^2+k^2}\right)$. $\mathbf{P}_{dt}^n$ can be obtained from:

$$\mathbf{P}_{dt}^n = \frac{1}{2}(\boldsymbol{a}^n \otimes \boldsymbol{w}^n + \boldsymbol{w}^n \otimes \boldsymbol{a}^n), \tag{8}$$

where $\boldsymbol{w}^n$ is the unit normal vector of shear plane, $\boldsymbol{a}^n$ is the vector of shear direction. λ^n, λ_0^n, $\boldsymbol{a}^n$, $\boldsymbol{w}^n$ of 24 CVPs in NiTi alloy are listed in Table 4.

Table 4
g=0.5846, *h*=0.8133, *k*=0.2804, *o*=0, *p*=0.271, *q*=0.729, *r*=1. [48]

n	$\boldsymbol{w_1^n}$	$\boldsymbol{w_2^n}$	$\boldsymbol{w_3^n}$	$\boldsymbol{a_1^n}$	$\boldsymbol{a_2^n}$	$\boldsymbol{a_3^n}$	$\boldsymbol{\lambda_0^n}$	$\boldsymbol{\lambda^n}$
1	-*g*	*o*	*h*	*o*	*k*	*o*	*p*	*r*
2	*o*	-*g*	-*h*	*k*	*o*	*o*	*p*	*r*
3	-*g*	*o*	-*h*	*o*	*k*	*o*	*p*	*r*
4	*o*	-*g*	*h*	*k*	*o*	*o*	*p*	*r*
5	-*g*	*o*	-*h*	*o*	*k*	*o*	*q*	*r*
6	*o*	-*g*	*h*	*k*	*o*	*o*	*q*	*r*
7	-*g*	*o*	*h*	*o*	*k*	*o*	*q*	*r*
8	*o*	-*g*	-*h*	*k*	*o*	*o*	*q*	*r*
9	-*h*	-*g*	*o*	*o*	*o*	*k*	*p*	*r*
10	-*h*	*g*	*o*	*o*	*o*	*k*	*q*	*r*
11	-*h*	*o*	-*g*	*o*	*k*	*o*	*p*	*r*
12	-*h*	*o*	*g*	*o*	*k*	*o*	*q*	*r*
13	*h*	*g*	*o*	*o*	*o*	*k*	*p*	*r*
14	-*h*	-*g*	*o*	*o*	*o*	*k*	*q*	*r*
15	-*h*	*o*	*g*	*o*	*k*	*o*	*p*	*r*
16	-*h*	*o*	-*g*	*o*	*k*	*o*	*q*	*r*
17	*g*	-*h*	*o*	*o*	*o*	*k*	*q*	*r*
18	-*g*	-*h*	*o*	*o*	*o*	*k*	*p*	*r*
19	*o*	-*h*	-*g*	*k*	*o*	*o*	*p*	*r*
20	*o*	-*h*	*g*	*k*	*o*	*o*	*q*	*r*
21	-*g*	-*h*	*o*	*o*	*o*	*k*	*q*	*r*
22	*g*	-*h*	*o*	*o*	*o*	*k*	*p*	*r*
23	*o*	-*h*	*g*	*k*	*o*	*o*	*p*	*r*
24	*o*	-*h*	-*g*	*k*	*o*	*o*	*q*	*r*

The detwinning strain tensor of (010) compound twin $\varepsilon_{Compound}$ can be determined by [45]:

$$\varepsilon_{Compound} = \xi\lambda R\frac{1}{2}s(\boldsymbol{m}\otimes\boldsymbol{n}+\boldsymbol{n}\otimes\boldsymbol{m})R^T, \quad (9)$$

where $\boldsymbol{m}$ and $\boldsymbol{n}$ are unit normal vector of habit plane and unit vector of twinning direction respectively. s is the shear magnitude and ξ is the volume fraction of the compound twin in the matrix. λ is the amount of transition by detwinning [47]. Details are listed in Table 5 [46].

Table 5

$\boldsymbol{m_1}$	$\boldsymbol{m_2}$	$\boldsymbol{m_3}$	$\boldsymbol{n_1}$	$\boldsymbol{n_2}$	$\boldsymbol{n_3}$	$\boldsymbol{s}$	$\boldsymbol{\lambda}$
0	0	1	1	0	0	0.238	0.5

Assuming the volume fraction of two detwinning modes satisfies the normalized condition: $\xi+\sum_{n=1}^{24}\xi^n=1$, and $\xi^i=\xi^j\ (i,j=1,\ 2,\ 3,\ldots,24)$ [48]. The value of ξ and ξ^n can be calibrated by fitting the average detwinning strains of the two modes, i.e. 6.79% for <011> Type II and 2.98% for

(001) compound [47], to the macroscopic recoverable strain of the two samples. The calibrated values are listed in Table 6. Thereby the pseudo-plastic strain ε_r can be obtained by combining Eq. 5, 6 and 9:

$$\varepsilon_r = \sum_{n=1}^{24} \xi^n (\lambda^n - \lambda_0^n) R \mathbf{P}_{dt}^n R^T + \xi \lambda R \frac{1}{2} s(\boldsymbol{m} \otimes \boldsymbol{n} + \boldsymbol{n} \otimes \boldsymbol{m}) R^T. \quad (10)$$

The plastic strain is permanent whose value can only increase. At maximum ε_t, the values of ε_r and ε_e are known, hence the plastic strain of each variant: $\varepsilon_p = \varepsilon_t - \varepsilon_r - \varepsilon_e$.

Upon unloading, the lattice strain changes freely in such a way to accommodate the difference between total strain and other strain components: $\varepsilon_e = \varepsilon_t - \varepsilon_r - \varepsilon_p$.

During shape recovery, the instant pseudo-plastic strain (ε_r') of each variant gradually recovers, whose value is related to the macroscopic recovered strain:

$$\varepsilon_r' = \varepsilon_r \cdot (\frac{\varepsilon - \Delta\varepsilon}{\varepsilon}) = \varepsilon_r \cdot (\frac{\varepsilon - \varepsilon_m + \varepsilon_t}{\varepsilon}), \quad (11)$$

where ε_r is the pseudo-plastic strain before shape recovery obtained from Eq. 10. ε is the macroscopic recoverable strain obtained from the macroscopic stress-strain curve (Fig. 4). $\Delta\varepsilon$ is the change in macroscopic strain during shape recovery. ε_m is the macroscopic strain before shape recovery. Similarly, the lattice strain can be obtained from: $\varepsilon_e = \varepsilon_t - \varepsilon_r' - \varepsilon_p$. Arising from grain boundaries and textures, the intergranular constraint is found to retard the shape recovery in polycrystalline NiTi [49]. Hence the gradient of lattice strain evolution is multiplied by k, representing the average intergranular constraint from the matrix:

$$\frac{d\varepsilon_e'}{d\varepsilon_t} = k \frac{\partial \varepsilon_e}{\partial \varepsilon_t}, \quad (12)$$

where ε_e' is the lattice strain predicted by the model. The calibrated parameters are listed in Table 6.

Table 6

Sample Condition	ξ	ξ^n	ε_m	ε	k
AC	0.35	0.027	6.11	5.46	0.03
HS	0.26	0.031	6.53	5.81	0.04

The calibrated value of ξ and ξ^n indicates that the amount of compound twin in AC NiTi is higher

than that in HS NiTi, which well agrees the observation in section 3.3.4 that more grains in AC NiTi are reoriented with [010] parallel to the AD so as to accommodate the detwinning strain. Texture effect is considered in the model via the anisotropic elastic property of variant (E_{hkl}), which is quantified by EPSC in section 3.3.3. The lower value of k in AC NiTi implies that random texture induces stronger intergranular constraint, consistent with observations from [49].

The comparison between experiment and proposed model are shown in Fig. 16. The loading process described by the model well fits the data since the elastic properties of variants are given in section 3.3.2. The novelty of the proposed model comes to the quantification of lattice strain evolution during the unloading and shape recovery. Upon unloading, lattice strain depends on the plastic and pseudo-plastic strain calculated at maximum stress level. During shape recovery, the instant pseudo-plastic strain of variant is estimated, thereby the lattice strain being calculated. It can be seen that lattice strain evolution of variant is linear, either positive or negative. The positive ones, for instance the (100) variant of AC NiTi, indicate that the strain recovery of that variant is larger than the average matrix, so that the difference in strain between the variant and matrix has to be compensated by the increasing of elastic lattice strain. And vice versa. Although concise as it is, the model effectively captures the overall trend of the texture-dependent lattice strain evolution in different variants, particularly the unloading and shape recovery process.

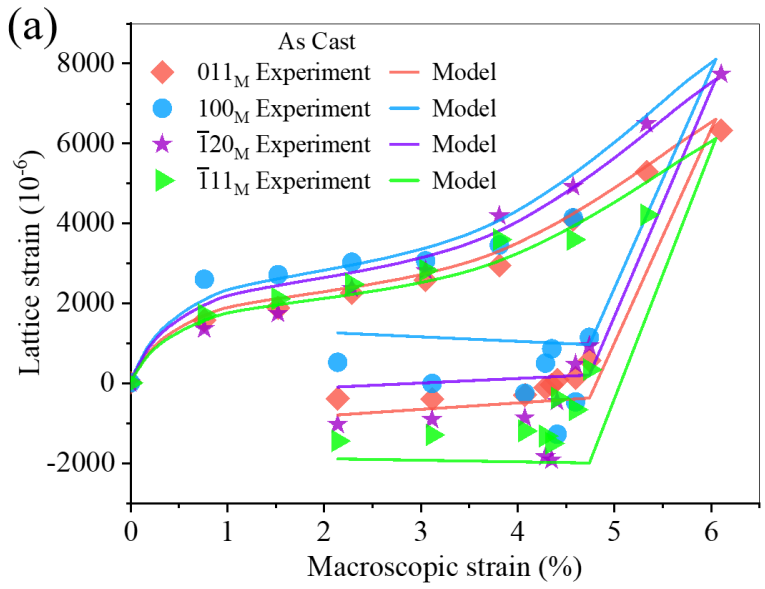

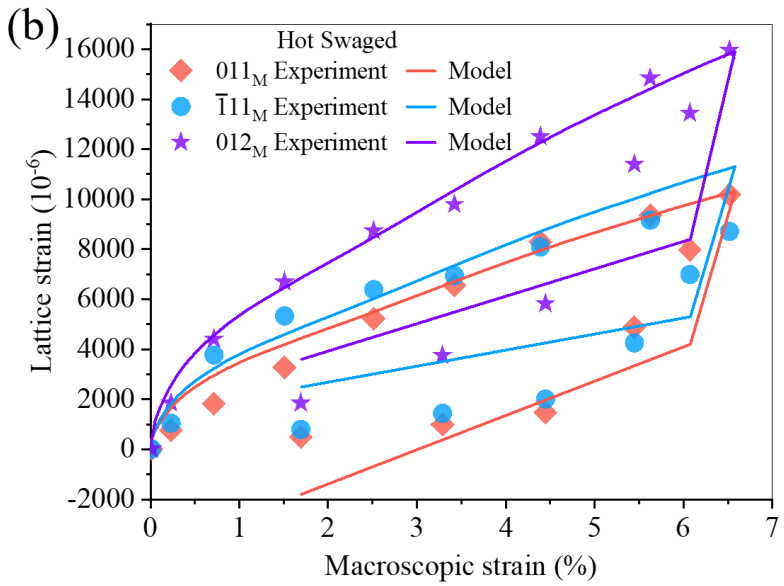

Fig. 16. Lattice strain evolution: comparison between experiment and proposed model. Uncertainties are comparable or smaller than the size of plotted symbols.

4. Summary and conclusions

This work has provided insight into the effect of texture introduced by different processing methods on the SME behaviour of variants as they exist in bulk polycrystalline NiTi alloys. Attentions were drawn to various properties of NiTi alloy, namely, grain morphology, microstrain, thermal expansion coefficient, lattice strain evolution, elastic properties and texture evolution. Based upon the experimental results, a multi-variant model that quantifies the lattice strain evolution during SME was constructed, shedding light on the degradation of functional behaviour from a mesoscopic point of view.

Conclusions are summarised as below:

Hot swaging process brings about reduction in grain dimension along RD, increase in microstrain, and formation of <010> fibre texture along AD.

The linearity of lattice strain evolution during stress-free thermal cycling suggests the accommodative nature of M phase to minimise the intergranular stress between M and A grains. The thermal expansion of M and A variants are demonstrated to be weakly affected by the texture.

The elastic response of variants show large extent of anisotropy. Elastic properties of both variants and macroscopic averaged value of AC, HS, HD samples lie within the range for single crystal state (the highest stiffness) and twinned structure (the lowest stiffness). Attributed to the texture effect, the same *hkl* variant in AC, HS and HD NiTi exhibits distinct elastic modulus. Texture and grain morphology effect on elastic properties are quantified by EPSC approach.

Major part of texture evolution during SME takes place within the region of stress-plateau. The rearranged texture retained upon unloading. Although AC, HS and HD NiTi presents different microstructure initially, the way of texture rearrangement are similar such that the [010] direction is reoriented parallel to the loading axis, thus accommodating the detwinning strain of (001) & (100) compound twins.

Being the likely first attempt so far, the proposed multi-variant model well captures the overall trend of the anisotropic lattice strain evolution during SME. The proportion of three strain modes of a variant largely depends on the orientation and texture. Random texture is found to induce more intergranular constraint during shape recovery.

Apart from the new findings, conclusions in the present work well match those from literature.

Data availability

The processed data used to support the conclusions of this study are included within the article. The raw data will be made available upon request.

Acknowledgements

AMK wishes to acknowledge the support of EPSRC through grants EP/S005072/1 and EP/P005381/1. Dr. Lenka Kuncicka and Prof. Radim Kocich acknowledge the financial support of the 19-15479S Project of the Grant Agency of the Czech Republic. We gratefully acknowledge the Science and Technology Facilities Council (STFC) for access to neutron beamtime RB1920246 at the ISIS Pulsed Neutron and Muon Source.

References

[1] Z. Wang, A.M. Korsunsky, Effect of Temperature on Shape Memory Materials, in: Reference Module in Materials Science and Materials Engineering, Elsevier Inc., 2020. https://doi.org/10.1016/B978-0-12-803581-8.11793-X.

[2] T.M. Brill, S. Mittelbach, W. Assmus, M.Mullner, B. Luthi, Elastic properties of NiTi, J. Condens. Matter Phys. 4 (1991) 9621-9627. https://doi.org/10.1088/0953-8984/3/48/004.

[3] M.F.-X. Wagner, W. Windl, Lattice stability, elastic constants and macroscopic moduli of NiTi martensites from first principles, Acta Mater. 56 (2008) 6232-6245. https://doi.org/10.1016/j.actamat.2008.08.043.
[4] S. Qiu, B. Clausen, S.A. Padula II, R.D. Noebe, R. Vaidyanathan, On elastic moduli and elastic anisotropy in polycrystalline martensitic NiTi, Acta Mater. 59 (2011) 5055-5066. https://doi.org/10.1016/j.actamat.2011.04.018.
[5] J. Wang, H. Sehitoglu, Martensite modulus dilemma in monoclinic NiTi-theory and experiments, Int. J. Plast. 61 (2014) 17-31. https://doi.org/10.1016/j.ijplas.2014.05.005.
[6] T. Ezaz, H. Sehitoglu, H.J. Maier, Energetics of twinning in martensitic NiTi, Acta Mater. 59 (2011) 5893-5904. https://doi.org/10.1016/j.actamat.2011.05.063.
[7] T. Ezaz, H. Sehitoglu, Type II detwinning in NiTi, Appl. Phys. Lett. 98 (2011) 141906. https://doi.org/10.1063/1.3574775.
[8] S.C. Mao, J.F. Luo, Z. Zhang, M.H. Wu, Y. Liu, X.D. Han, EBSD studies of the stress-induced B2-B19' martensitic transformation in NiTi tubes under uniaxial tension and compression, Acta Mater. 58 (2010) 3357-3366. https://doi.org/10.1016/j.actamat.2010.02.009.
[9] Y. Liu, Z. Xie, J.Van Humbeeck, L. Delaey, Effect of texture orientation on the martensite deformation of NiTi shape memory alloy sheet, Acta Mater. 47 (1999) 645-660. https://doi.org/10.1016/S1359-6454(98)00376-0.
[10] Y. Liu, Z. Xie, J.Van Humbeeck, L. Delaey, Some results on the detwinning process in NiTi shape memory alloys, Scr. Mater. 41 (1999) 1273-1281. https://doi.org/10.1016/S1359-6462(99)00299-7.
[11] O. Benafan, R.D. Noebe, S.A. Padula II, D.W. Brown, S. Vogel, R. Vaidyanathan, Thermomechanical cycling of a NiTi shape memory alloy-macroscopic response and microstructural evolution, Int. J. Plast. 56 (2014) 99-118. https://doi.org/10.1016/j.ijplas.2014.01.006.
[12] Z. Wang, J. Everaerts, E. Salvati, A.M. Korsusnky, Evolution of thermal and mechanical properties of Nitinol wire as a function of ageing treatment conditions, J. Alloys Compd. 819 (2020) 153024. https://doi.org/10.1016/j.jallcom.2019.153024.
[13] Z. Zheng, C. Hu, L. Cai, X. Chen, F. Jing, First-principles determination of the structure, elastic constant, phase diagram and thermodynamics of NiTi alloy, Physica B 405 (2010) 3665-3672. https://doi.org/10.1016/j.physb.2010.05.062.
[14] B. Ye, B.S. Majumadar, I. Dutta, Texture development and strain hysteresis in a NiTi shape-memory alloy during thermal cycling under load, Acta Mater. 57 (2009) 2403-2417. https://doi.org/10.1016/j.actamat.2009.01.032.
[15] C. Yu, B. Aoun, L. Cui, Y. Liu, H. Yang, X. Jiang, S. Cai, D. Jiang, Z. Liu, D.E. Brown, Y. Ren, Synchrotron high energy X-ray diffraction study of microstructure evolution of severely cold drawn NiTi wire during annealing, Acta Mater. 115 (2016) 35-44. https://doi.org/10.1016/j.actamat.2016.05.039.
[16] P. Sedmak, P. Sittner, J. Pilch, C. Curfs, Instability of cyclic superelastic deformation of NiTi investigated by synchrotron X-ray diffraction, Acta Mater. 94 (2015) 257-270. https://doi.org/10.1016/j.actamat.2015.04.039.
[17] R. Kocich, L. Szurman, M. Kursa, The methods of preparation of Ti-Ni-X alloys and their forming, Shape Memory Alloys-Processing, Characterization and Applications, Croatia: InTech, pp.27-52. http://dx.doi.org/10.5772/50067.
[18] G. Laplanche, T. Birk, S. Schneider, J. Frenzel, G. Eggler, Effect of temperature and texture on the reorientation of martensite variants in NiTi shape memory alloys, Acta Mater. 127 (2017) 143-152.

https://doi.org/10.1016/j.actamat.2017.01.023.
[19] O. Benafan, R.D. Noebe, S.A. Padual II, A. Garg, B. Clausen, S. Vogel, Temperature dependent deformation of the B2 austenite phase of a NiTi shape memory alloy, Int. J. Plast. 51 (2013) 103-121. https://doi.org/10.1016/j.ijplas.2013.06.003.
[20] E.S. Statnik, A.I. Salimon, C. Besnard, J. Chen, Z. Wang, T. Moxham, I.P. Dolbnya, A.M. Korsunsky, Ovine Bone Morphology and Deformation Analysis Using Synchrotron X-ray Imaging and Scattering, Quantum Beam Sci. 4 (2020) 29. https://doi.org/10.3390/qubs4030029.
[21] F. Uzun, A.I. Salimon, E.S. Statnik, C. Besnard, J. Chen, T. Moxham, Z. Wang, A.M. Korsunsky, Polar transformation of 2D X-ray diffraction patterns and the experimental validation of the hDIC technique, Measurement 151 (2020) 107193. https://doi.org/10.1016/j.measurement.2019.107193.
[22] L. Kuncicka, R. Kocich, Deformation behaviour of Cu-Al clad composites produced by rotary swaging, IOP Conf. Ser. Mater. Sci. Eng. 369 (2018) 012029. https://doi.org/10.1088/1757-899X/369/1/012029.
[23] R. Kocich, M. Kursa, I. Szurman, A. Dlouhy, The influence of imposed strain on the development of microstructure and transformation characteristics of Ni-Ti shape memory alloys, J. Alloys Compd. 509 (2011) 2716-2722. https://doi.org/10.1016/j.jallcom.2010.12.003.
[24] R. Kocich, L. Kuncicka, P. Kral, P. Strunz, Characterization of innovative rotary swaged Cu-Al clad composite wire conductors, Mater. Des. 160 (2018) 828–835. https://doi.org/10.1016/j.matdes.2018.10.027.
[25] R. Kocich, L. Kuncicka, D. Dohnalik, A. Machackova, M. Sofer, Cold rotary swaging of a tungsten heavy alloy: Numerical and experimental investigations, Int. J. Refract. Met. Hard Mater. 61 (2016) 264–272. https://doi.org/10.1016/j.ijrmhm.2016.10.005.
[26] J.R. Santisteban, M.R. Daymond, J.A. James, L. Edwards, ENGIN-X: a third-generation neutron strain scanner, J. Appl. Cryst. 39 (2006) 812-825. https://doi.org/10.1107/S0021889806042245.
[27] F. Uzun, C. Papadaki, Z. Wang, A.M. Korsunsky, Neutron strain scanning for experimental validation of the artificial intelligence based eigenstrain contour method, Mech. Mater. 143 (2020) 103316. https://doi.org/10.1016/j.mechmat.2020.103316.
[28] H.M. Rietveld, A profile refinement method for nuclear and magnetic structures, J. Appl. Cryst. 2 (1969) 65-71. https://doi.org/10.1107/S0021889869006558.
[29] A.C. Larson, R.B. Von Dreele, General structure analysis system, Los Alamos National Laboratory Report LAUR (1994) 86-748. https://personal.ems.psu.edu/~ryba/coursework/Advanced%20Powder%20Diffraction/GSASManual.pdf.
[30] H. Sitepu, Texture and structural refinement using neutron diffraction data from molybdite (MoO3) and calcite (CaCO3) powders and a Ni-rich Ni50.7Ti49.3 alloy, Powder Diffr. 24 (2009) 315-326. https://doi.org/10.1154/1.3257906.
[31] N. Hatcher, O.Y. Kontsevoi, A.J. Freeman, Role of elastic and shear stabilities in the martensitic transformation path of NiTi, Phys. Rev. B 80 (2009) 144203. https://doi.org/10.1103/PhysRevB.80.144203.
[32] E. Oliver, J. Santisteban, J. James, M. Daymond, J. Dann, ENGIN-X user manual, isis.stfc.ac.uk (2004). https://www.isis.stfc.ac.uk/Pages/engin-x-manual6870.pdf.
[33] Z. Wang, J. Chen, C. Besnard, A.M. Korsunsky, Microstructure evolution in a severely cold-worked NiTi wire during ageing treatment: An in situ neutron diffraction study, Mater. Lett. 281 (2020) 128676. https://doi.org/10.1016/j.matlet.2020.128676.

[34] F. Bachmann, R. Hielscher, H. Schaeben, Texture analysis with MTEX-Free and open source software toolbox, Solid State Phenom. 160 (2010) 63-68. https://doi.org/10.4028/www.scientific.net/SSP.160.63.
[35] Y. Zhao, J. Zhang, Microstrain and grain-size analysis from diffraction peak width and graphical derivation of high-pressure thermomechanics, J. Appl. Cryst. 41 (2008) 1095-1108. http://dx.doi.org/10.1107/S0021889808031762.
[36] T. Ungar, I. Dragomir, A. Revesz, A. Borbely, The contrast factors of dislocations in cubic crystals: the dislocation model of strain anisotropy in practice, J. Appl. Cryst. 32 (1999) 992-1002. https://doi.org/10.1107/S0021889899009334.
[37] S. Qiu, V.B. Krishnan, S.A. Padula, R.D. Noebe, D.W. Brown, B. Clausen, R. Vaidyanathan, Measurement of the lattice plane strain and phase fraction evolution during heating and cooling in shape memory NiTi, Appl. Phys. Lett. 95 (2009) 141906. https://doi.org/10.1063/1.3245308.
[38] J.F. Nye, Physical properties of crystals, Oxford: Clarendon Press (1985).
[39] Y. Liu, Z. Xie, J.Van Humbeeck, L. Delaey, Some results on the detwinning process in NiTi shape memory alloys, Scr. Mater. 41 (1999) 1273-1281. https://doi.org/10.1016/S1359-6462(99)00299-7.
[40] S. Rajagopalan, A.L. Little, M.A.M. Bourke, R. Vaidyanathan, Elastic modulus of shape-memory NiTi from in situ neutron diffraction during macroscopic loading, instrumented indentation, and extensometry, Appl. Phys. Lett. 86 (2005) 081901. https://doi.org/10.1063/1.1863437.
[41] B. Clausen, C.N. Tome, D.W. Brown, S.R. Agnew, Reorientation and stress relaxation due to twinning: Modeling and experimental characterization for Mg, Acta Mater. 56 (2008) 2456-2468.
[42] P. Chowdhury, H. Sehitoglu, Deformation physics of shape memory alloys – Fundamentals at atomistic frontier, Prog. Mater. Sci. 88 (2017) 49-88. https://doi.org/10.1016/j.pmatsci.2017.03.003.
[43] Y. Liu, Z. Xie, Detwinning in shape memory alloy, in: P.L. Reece, Progress in Smart Materials and Structures 3, Nova Science Publishers Inc., 2007, pp. 29-65.
[44] S. Cai, J.E. Schaffer, Y. Ren, C. Yu, Texture evolution during nitinol martensite detwinning and phase transformation, Appl. Phys. Lett. 103 (2013) 241909. https://doi.org/10.1063/1.4846495.
[45] K. Gall, H. Sehitoglu, Y.I. Chumlyakov, I.V. Kireeva, Tension-compression asymmetry of the stress-strain response in aged single crystal and polycrystalline NiTi, Acta Mater. 47 (1999) 1203-1217. https://doi.org/10.1016/S1359-6454(98)00432-7.
[46] O. Matsumoto, S. Miyazaki, K. Otsuka, H. Tamura, Crystallography of martensitic transformation in Ti-Ni single crystals, Acta Metall. 35 (1987) 2137-2144. https://doi.org/10.1016/0001-6160(87)90042-3.
[47] Q.S. Zheng, Y. Liu, Prediction of the detwinning anisotropy in textured NiTi shape memory alloy, Philos. Mag A 82 (2002) 665-683. https://doi.org/10.1080/01418610208243195.
[48] C. Yu, G. Kang, Q. Kan, Crystal plasticity based constitutive model of NiTi shape memory alloy considering different mechanisms of inelastic deformation, Int. J. Plast. 54 (2014) 132-162. https://doi.org/10.1016/j.ijplas.2013.08.012.
[49] K. Gall, T.J. Lim, D.L. McDowell, H. Sehitoglu, Y.I. Chumlyakov, The role of intergranular constraint on the stress-induced martensitic transformation in textured polycrystalline NiTi, Int. J. Plast. 16 (2000) 1189-1214. https://doi.org/10.1016/S0749-6419(00)00007-3.